Published in final edited form as:
J Magn Reson Imaging. 2011 February ; 33(2): 372–381. doi:10.1002/jmri.22439.

Performance of μMRI-Based Virtual Bone Biopsy for Structural and Mechanical Analysis at the Distal Tibia at 7T Field Strength

Yusuf A. Bhagat, PhD, **Chamith S. Rajapakse, PhD**, **Jeremy F. Magland, PhD**, **James H. Love, AS**, **Alexander C. Wright, PhD**, **Michael J. Wald, MSEE**, **Hee Kwon Song, PhD**, and **Felix W. Wehrli, PhD**
Laboratory for Structural NMR Imaging, Department of Radiology, University of Pennsylvania, MRI Education Center, 1 Founders, 3400 Spruce Street, Philadelphia, PA 19104

Abstract

Purpose—To assess the performance of a 3D fast spin echo (FSE) pulse sequence utilizing out-of-slab cancellation through phase alternation and micro magnetic resonance imaging (μMRI) based virtual bone biopsy processing methods to probe the serial reproducibility and sensitivity of structural and mechanical parameters of the distal tibia at 7.0T.

Materials and Methods—The distal tibia of five healthy subjects was imaged at three time-points with a 3D FSE sequence at 137×137×410 μm^3 voxel size. Follow-up images were retrospectively 3D registered to baseline images. Coefficients of variation (CV) and intraclass correlation coefficients (ICC) for measures of scale and topology of the whole tibial trabecular bone (TB) cross-section as well as finite-element derived Young's and shear moduli of central cuboidal TB sub-volumes ($8 \times 8 \times 5\ mm^3$) were evaluated as measures of reproducibility and reliability. Four additional cubic TB sub-regions (anterior, medial, lateral and posterior) of similar dimensions were extracted and analyzed to determine associations between whole cross-section and sub-regional structural parameters.

Results—Mean SNR over the fifteen image acquisitions was 27.5 ± 2.1. Retrospective registration yielded an average common analysis volume of 67% across the 3 exams per subject. Reproducibility (mean CV=3.6%; range, 1.5–5%) and reliability (ICCs, 0.95–0.99) of all parameters permitted parameter-based discrimination of the five subjects in spite of the narrow age range (26–36 years) covered. Parameters characterizing topology were better able to distinguish two individuals who demonstrated similar values for scalar measurements (~34% difference, $p<0.001$). Whole-section axial stiffness encompassing the cortex was superior at distinguishing 2 individuals relative to its central sub-regional TB counterpart (~8% difference; $p<0.05$). Inter-region comparisons showed that although all parameters were correlated (mean $R^2 = 0.78$; range 0.57 to 0.99), the strongest associations observed were those for the erosion index (mean $R^2 = 0.95$, $p \leq 0.01$).

Conclusion—The reproducibility, and structural and mechanical parameter-based discriminative ability achieved in five healthy subjects suggests that 7T-derived μMRI of TB can be applied towards serial patient studies of osteoporosis and may enable earlier detection of disease or treatment-based effects.

Corresponding Author: Felix W. Wehrli, PhD, Laboratory for Structural NMR Imaging, Department of Radiology, University of Pennsylvania, MRI Education Center, 1 Founders, 3400 Spruce Street, Philadelphia, PA 19104, Tel: 215-662-7951, Fax: 215-662-7263, wehrli@mailed.upenn.edu.

Keywords

Ultra High Field MRI; 7.0T, Fast Spin Echo; Trabecular Bone; Digital Topological Analysis; Finite Element Analysis

INTRODUCTION

Quantitative evaluation of macro- and microstructural properties of bone enhance our ability to estimate bone strength in degenerative disorders as in osteoporosis (1,2). Bone mineral density (BMD), a ubiquitous parameter typically assessed via dual energy X-ray absorptiometry, is most typically used as a surrogate of bone strength in osteoporotic individuals (3). However, BMD does not provide insights into bone quality, a secondary marker relaying bone strength and risk of fracture through interrogation of trabecular and cortical bone microarchitecture (4). Advances in 3D micro-magnetic resonance imaging (μMRI) allow direct visualization and quantification of trabecular bone (TB) architecture serially during senescence, disease progression and regression in response to treatment, and for fracture discrimination and prediction (5,6). The virtual bone biopsy (VBB), a μMRI based suite of image acquisition and processing techniques enables quantification of TB architectural properties at peripheral skeletal sites such as the distal tibia and radius (7). Additionally, finite element (FE) analysis applied to FE meshes generated from high resolution *in* vivo μMRI can directly gauge the mechanical implications of structural changes (8,9) in response to intervention.

Since the thickness of human bone trabeculae is on the order of 100–150 μm, the detection of subtle microstructural TB alterations such as the conversion of plates to rods relies on adequate signal-to-noise ratio (SNR), which intrinsically governs the permissible spatial resolution and scan time. Currently, images of peripheral anatomical locations such as the distal tibia can be acquired in as rapidly as 5–15 minutes with the in-plane resolution and slice thickness ranging from 137–190 μm^2 and 160–1500 μm, respectively, at 1.5T and 3.0T (10–12).

With the emergence of ultra-high field (UHF; ≥7.0T) whole-body scanners, quantification of the TB microstructure is likely to benefit from the expected SNR gain (13,14), with one early report citing an SNR increase by a factor of 1.9 over 3.0T-based TB images of the distal tibia (15). Nonetheless, questions surrounding the use of optimal pulse sequences for imaging TB microarchitecture within the constraints of specific absorption limits, while harnessing the enhanced SNR to improve spatial resolution remain to be explored. Enhancements in SNR can be applied towards improving image resolution (e.g. achieving isotropic instead of the usual anisotropic resolution) without incurring excessive SNR penalties (16), or alternatively to reduce scan time in conjunction with parallel imaging (17). Improved SNR may enhance detection sensitivity, which would be of particular benefit in longitudinal assessments of TB microstructural integrity potentially allowing earlier and more accurate assessments of structural and mechanical changes following therapeutic interventions.

Here, we have investigated the reliability of TB parameters derived from the VBB-based digital topological and FE analyses in healthy subjects using a recently developed 3D fast spin echo with-out-of-slab cancellation (FSE-OSC) technique through phase alternation (18) designed for TB structural imaging at 7.0T, operating within the specific absorption rate (SAR) constraints (19). Three dimensional FSE sequences have become a popular choice for a wide array of clinical applications (20) encompassing brain (21) and musculoskeletal (22) imaging. The primary advantage of spin-echo type sequences over the more commonly

utilized balanced steady state free precession (bSSFP) (13–15) sequences for TB imaging is their lower sensitivity to off-resonance effects arising from susceptibility differences at the bone and bone marrow interface (23,24). The FSE-OSC sequence developed previously (18) utilizes A) a slab-selective excitation pulse, B) low RF-power depositing non-selective refocusing pulses, C) phase alternation to cancel undesired out-of-slab signal and D) a higher readout bandwidth (108 Hz/pixel) to cover the broadened lipid spectrum at 7T thereby yielding a narrower point spread function in the readout direction (18). Another objective of this work involved an assessment of the custom designed RF coils and ankle immobilization device for routine serial imaging of the distal tibia at 7.0T. Our overall goal was to minimize scan-to-scan inconsistencies (coil positioning, motion degradation, registration) to maximize reproducibility of the structural and mechanical parameters that relay TB microarchitectural information and therefore improve discriminating power.

METHODS

Image Acquisition, Reconstruction and Preprocessing

All studies were performed on a Siemens 7.0T whole-body scanner (Siemens Medical Systems, Erlangen, Germany) equipped with gradients of maximum amplitude and slew rate of 45 mT/m and 200 T/m/s, respectively. Five healthy males (ages, 26–36 years) provided informed consent in accordance with study guidelines of an institutional review board. The left distal tibia of each subject was scanned 3 times (baseline, follow-up 1 and follow-up 2) over a 3-month period, with a 1-week minimum duration between successive examinations.

A depiction of the setup of the RF coils along with the positioning device is given in Figure 1. The transmit-receive arrangement consisted of a Helmholtz pair transmit (Tx) coil and 4-element phased array receive coil (horseshoe geometry, 4×4 cm^2 loops) operating at 297.2 MHz (Insight MRI, Worcester, MA) (18,25). These coils were arranged in a compact assembly to afford reproducible ankle and foot immobilization.

The protocol consisted of axial and sagittal 2D gradient echo localizers (1min 16s) to ensure optimal coil placement relative to the tibial end-plate and for prescription of the high resolution 3D FSE volume. The localizer scans were followed by a high resolution 3D FSE-OSC sequence (18) performed with: TR/TE= 500/20 ms, 8 echoes per TR, 4 shots, variable flip angle refocusing pulses (linearly decreasing from 180° to 90°) to operate within SAR limits, RF pulse BW=3.0 KHz, readout BW= 108 Hz/pixel, R>L phase encoding (PE), 60% partial Fourier along the PE direction (Y), segmented PE in Z, 8 echoes (centric ordering) × 4 interleaves= 32 encodings, FOV= $63 \times 63 \times 13$ mm^3 and a $460 \times 460 \times 32$ data array yielding a resolution of $137 \times 137 \times 410$ μm^3. The interecho spacing was 20 ms in order to accommodate a refocusing pulse duration of 1 ms and gradient amplitudes of 20 mT/m. Total acquisition time was 10min 44s with parallel imaging (GRAPPA, R=1.8) using multicolumn, multiline interpolation (26) as described previously (16).

An important feature of the 3D FSE-OSC sequence is its utilization of phase alternation to cancel undesired out-of-slab signal (18). As mentioned earlier, the 90° RF excitation pulse is slab-selective, whereas the refocusing RF pulses are non-selective. Ordinarily, this would lead to severe artifacts due to even minor B1 field inhomogeneities, given that spurious magnetization is excited outside the imaging slab. As a solution, every phase encoding line is acquired twice with the phase of the selective excitation pulse alternating between 0° and 180° and the phase of each refocusing pulse kept constant at 90° relative to the initial excitation. Prior to reconstruction, the data are combined by subtracting every other line to enable the desired magnetization (excited by the initial selective pulse) to be combined constructively, and out-of-slab magnetization to be cancelled.

The images were subsequently corrected for subject motion during the scan via autofocusing (27), a retrospective correction method for translational and rotational displacements, performed in k-space. Here, we used the algorithm by Lin *et al.* (28) applied to correct for in-plane translations, in conjunction with optimizing a focus criterion to determine the effectiveness of the correction.

Post-processing and Analyses

Figure 2 provides an overview of the image co-registration, post-processing steps and analysis. The square-root sum-of-squares combined images were auto-masked by disconnecting the soft-tissue portion exterior to the periosteum. SNR was measured as the mean marrow signal intensity (within the masked TB region) divided by the mean of the signal-free region (signal and artifact free region of noise only). Subsequently, a retrospective registration method was employed by first computing 3D transformation parameters (3 rotations and 3 translations) for registering the follow-up to the baseline images (29). Prior to application of the transformation, the follow-up images were upsampled in k-space by a factor of 3 and subsequently downsampled again after mapping the images to the grid of the baseline images (Figure 2A and B). The resulting images then underwent bone volume fraction (BVF) mapping via generation of 3D grayscale maps in which pure bone was assigned an intensity of 100, pure marrow an intensity of zero (30).

The preprocessed BVF images underwent four sets of analyses. First, whole cross-sectional volumes including both TB and cortical bone (CB) were used to compute whole-bone axial stiffness (E_{zz}^{cs}) via μFE analysis involving simulated compression tests (31) (Figure 2C). Second, full cross-sectional TB regions were analyzed for parameters of scale and topology of the trabecular network (Figure 2D). Third, $8 \times 8 \times 5$ mm^3 parallelepiped-shaped volumes were extracted at the centroids of the TB regions for grayscale μFE analysis and for deriving structural parameters of scale and topology (32), to directly compare mechanical and structural measures (Figure 2D). The faces of the parallelepiped sub-volumes were aligned with the image coordinate axes, × (antero-posterior), y (medio-lateral) and z (infero-superior). Parameters of scale yield the size and thickness of trabecular elements whereas topological parameters portray the microarchitectural arrangement of the TB network. The latter were obtained by digital topological analysis (DTA) which classifies each voxel in a 3D structure as a surface, curve or junction type based on the connectivity information of the neighboring voxels (32). Fourth, subregional TB microarchitectural parameters were computed from four additional $8 \times 8 \times 5$ mm^3 subvolumes extracted at the anterior, medial, lateral and posterior regions for the purpose of interrogational comparison (Figure 2E).

Structural parameters were derived from the 3D BVF images, which yielded mean BVF (bone volume/total volume) as ΣBVF_i where BVF_i is the fractional occupancy of bone in the *ith* voxel, summed over all voxels within the selected region. Trabecular thickness (Tb. Th, μm) was computed with the fuzzy distance transform (FDT) method (33), which yields trabecular thickness in the limited spatial resolution and SNR regime of in vivo mapping. Topological parameters are obtained via DTA after skeletonizing the BVF images (34) so that trabecular plates are converted to surfaces and trabecular rods to curves, yielding surface-to-curve (S/C) ratio (ratio of plate-like to rod-like trabeculae) and erosion index (EI, ratio of the sum of the parameters expected to increase with osteoclastic resorption to the sum of the parameters expected to decrease) (32) (Figure 2D (2–3)).

Micro-FE analysis was performed in accordance with the model outlined by Van Rietbergen *et al*. (35) using a FE solver reported previously (31). In brief, voxel-based finite-element meshes were created on the basis of the 3D BVF maps (excluding voxels with BVF<20%) by setting the material Young's modulus (YM) proportional to voxel BVF assuming a value

of 15 GPa for pure bone tissue and Poisson's ratio of 0.3 (16,31). Simulated axial compression and shear tests were then performed on the cuboid sub-volumes (Figure 2D6)). Whole-section axial stiffness comprising both trabecular bone and cortex were also computed as described previously (9) (Figure 2C (1–2)).

Statistics

Statistical analyses were performed using SigmaStat 4.0 (Aspire International Software, Ashburn, VA) and JMP 7.0 (SAS Institute Inc., Cary, NC). Coefficients of variation (CV) and intra-class correlation coefficients (ICC) served as metrics of reproducibility and reliability (36), respectively. Mean CVs representing a mean of the CVs computed per subject for each parameter reflected the global reproducibility of a given parameter. Analysis of variance was performed to assess the sensitivity of the 7T μMRI-based VBB method to discriminate subjects on the basis of the computed structural, topological and mechanical parameters. Inter-region and inter-parameter regression of structural parameters was performed and Pearson's correlation coefficients were determined.

RESULTS

Figure 3 provides a visual impression of the achieved reproducibility in one of the subjects studied across the 3 time points. Close similarity in TB regional network patterns on the images and topological classifications within the 3D rendered skeletonized cores can be appreciated across the time course suggesting effective registration. The retrospective autofocusing motion-correction method detected within-scan translational shifts from 1 to 7 pixels (137 μm to 960 μm) in 6 out of the total 15 scans, in qualitative agreement with the improvement in visually perceived image sharpness. The data suggest robust immobilization and set-up reproducibility and a high level of subject compliance for serial scans. Mean SNR over the 15 anisotropic image acquisitions was 27.5 ± 2.1, corresponding to improvements by factors of 1.6 and 3.0 over 3.0T and 1.5T derived FSE-OSC distal tibia TB images with 4-element receive coils of identical design (18). Retrospective registration yielded an average common analysis volume of 67% across the 3 exams per subject.

The reproducibility data in the form of ranges, means, CVs and ICCs for whole tibial cross-section parameters of scale (BVF, Tb.Th) and topology (S/C and EI), whole section (TB +CB) axial stiffness and central sub-regional ($8 \times 8 \times 5$ mm^3) elastic and shear moduli for all 5 subjects are given in Table 1. ICCs ranged from 0.95 to 0.99 for all parameters with average CVs ranging from 1.5% to 4.9% (mean = 3.6%), indicative of a high level of reproducibility achievable with the 3D FSE-OSC sequence utilizing the new UHF-based coils, setup and post-processing methods. Measures of topology (S/C and EI) were more reproducible (CVs 3% and 2.4%) than other parameters such as BVF (4.4%) or elasticity (CVs 4.8 to 4.9%, Table 1). The rank order of the directional elastic moduli was consistent among the study subjects: E_{zz} (range, 1.01 to 1.44 GPa) > E_{yy} (range, 0.29 to 0.52 GPa) ≈ E_{xx} (range, 0.27 to 0.50 GPa). As expected, E_{zz} (modulus along the bone's major loading axis) was larger than elastic moduli for compressive loading in the medio-lateral and antero-posterior directions, commensurate with prior results (31). The reproducibility of the central sub-regional structural and DTA parameters (BVF, Tb.Th, S/C and EI) was on par with those derived from the whole tibial cross-section values with CVs ranging from 2.1% to 5.2% and ICCs from 0.93 to 0.99.

Scatterplots of select parameters from analysis of the full tibial cross-section highlight the discriminatory power of the technique despite the narrow age range (26–36 years) of participating subjects (Figure 4A–D). Figure 4E shows a scatterplot of the whole-section stiffness within the 5 subjects. Interestingly, topological parameters (S/C and EI) better discriminate (~34% difference, $p<0.001$) two individuals (subjects 1 and 2) where similar

mean BVF (9.8 ± 0.4% and 9.8 ± 0.8%; Figure 4) and Tb.Th values (105±1.4 μm and 103±1.9 μm) are observed. A similar trend was noted when comparing results of the sub-regional analysis between the same two subjects (Figure 5). S/C and EI demonstrated significant mean differences of 21% and 17% ($p<0.05$), respectively between subjects 1 and 2 in spite of the similarities in BVF and Tb.Th. Along these lines, on average, whole-section stiffness encompassing cortical bone (Figure 4E) was noted to be superior in its discriminating ability between subjects 1 and 2 (~9% difference, $p=0.03$), and between subjects 3 and 5 (8% difference, $p=0.02$) compared to its sub-regional counterpart (Figure 5D).

Table 2 lists the results of the inter-region associations of the four structural parameters evaluated comparing the mean values computed for the entire trabecular cross-section with those in the five sub-regions. We note that all parameters are correlated (R^2 ranging from 0.57 to 0.99) even though not all correlations were significant (likely due to insufficient power). The strongest inter-region associations found were those for the erosion index (R^2 = 0.92 to 0.99, $p=0.01$ to $p<0.001$) whereas BVF was more weakly correlated (all $p>0.05$). For Tb.Th, only the lateral subregion was highly correlated ($R^2 = 0.99$; $p<0.01$) to its full cross-sectional analogue. The data suggest that properties characterizing topology and to some extent, thickness, appear to be preserved while BVF is a more regional property.

DISCUSSION

This study was designed to evaluate the reproducibility and reliability of structural and mechanical TB parameters derived from images obtained with a new 3D spin-echo pulse sequence at 7T. The main goal of performing such a study was to determine the feasibility of routine clinical imaging of the distal tibia at UHF for the assessment of bone integrity. The custom-built Helmholtz transmit and receive coils, together with an immobilization platform setup, was designed to minimize motion-induced image blurring, and thus scan-to-scan inconsistencies. The most notable findings of our study include: (1) good quality 3D FSE-OSC images with highly reproducible TB network-related features (Figures 2 and 3), (2) superior retrospective registration of follow-up to baseline volume (mean common analysis volume, 67% across 3 time points), (3) highly reproducible DTA and mechanical parameters (ICC range, 0.95 to 0.99; CV range, 1.5% to 4.9% (Table 1), and (4) the ability to discriminate individuals from a narrow age range on the basis of structural and mechanical parameters. With topological parameters having a reproducibility of 3%, our present 7 T imaging and processing technology should allow us to detect a temporal change of the same magnitude in response to treatment with as few as 10 subjects with 5% significance and 80% power.

It is interesting to note that topological parameters (S/C and EI) were more sensitive than BVF in detecting differences between individuals as observed (Figures 4c and d versus a). We note that the range from lowest to highest mean BVF was 30% as opposed to 81% and 90% for S/C and EI, respectively, thereby making such parameters better discriminators, which is reflected also by the ICC values (0.99 vs. 0.95 for BVF). Similar observations have previously been noted in the context of clinical osteoporosis where the range of changes in topological parameters far surpassed that of BVF (37,38).

Detectable changes of microstructural TB, such as the conversion of plates to rods, hinges on both SNR and resolution. Recent data suggest that trabecular plate perforations were detectable at isotropic but not at anisotropic resolution (comparing 160 × 160 × 160 μm^3 versus 137 × 137 × 410 μm^3 (16). However, the potential for detection of such small (but possibly clinically significant) detail cannot be realized unless adequate SNR is available to mitigate the SNR loss from reduced voxel size. SNR values at the currently practiced 137 ×

137 × 410 μm^3 voxel size in our study ranged from 24.5 to 30.5 within the 15 exams performed in the 5 subjects. Given that these values exceed those by a factor of about 3.1 relative to 1.5T (18), respectively, for comparable scan time and hardware set-up, one could afford to trade off some of the SNR to achieve isotropic voxels (160 × 160 × 160 μm^3), on the order of thickness of human bone trabeculae (39). We thus project that the 3D FSE-OSC sequence at 7T would yield SNR values ranging from 13.0 to 16.2 for this resolution regime for comparable scan time and volume. Initial data (not shown) confirm these projections (SNR range, 16.6 to 18.6). These SNR values are considerably above an adequate SNR level (~12) deemed necessary to detect a 5% change in either BVF or topological parameters (S/C and EI), as predicted in the work of Li *et al* (40).

The reproducibility of structural, topological and mechanical parameters in this study is superior to previous studies that have evaluated similar measures at peripheral sites (distal tibia and radius)(16,36,41). Previously, Newitt *et al.* (41) reported an average CV of 6.5% for structural and mechanical parameters (range, 2.4% to 9.3%) in a reproducibility study of the distal radius at 1.5T using a 3D gradient echo sequence with voxel sizes of 156 × 156 × 500 μm^3. Gomberg *et al.*(36) found a mean CV of 7.4% (range, 4.6% to 10%) and ICCs ranging from 0.68 to 0.97 for structural parameters in their reproducibility study of distal radii and tibiae at 1.5T using the 3D fast large-angle spin-echo (FLASE) sequence (42) for the same anisotropic voxel size as in our present protocol. In that study, translational and rotational motion-induced blurring and mismatch of the analysis volumes between baseline and follow-up scans were identified as the main sources of error. A recent reproducibility study by Wald *et al*. (16) at the distal tibia at 3.0T employing 3D FLASE at 137×137×410 μm^3 voxel size yielded an average CV of 3.3% (range, 1% to 5.2%) and ICCs from 0.93 to 0.99, remarkably similar to the values reported here using a FSE based sequence (mean CV 3.6%; Table 1). Nonetheless, the margin for sacrificing SNR to enhance resolution is far smaller at 3T than at 7T, therefore motivating the pursuit of such studies at UHF. We attribute the improved reproducibility and sensitivity in the present study to the substantially enhanced SNR achievable at UHF. In a study focused on simulations based on images derived from high-resolution micro-CT by downsampling to typical *in vivo* resolution and superimposing Rician noise to SNR levels characteristic of those achievable at 1.5T, Li *et al.* (40) predicted errors of up to 25% and 70% for BVF and S/C if the SNR of the repeat scan differed by 50% (e.g., 6.0 to 9.0). However, that work also showed that the errors become negligible at higher SNR levels such as those achieved in the present study.

With respect to the choice of an optimal pulse sequence for TB imaging at UHF, a spin-echo type sequence such as FLASE (typical acquisition time, 12–15 mins) exceeds acceptable SAR levels at 7T. FLASE employs two high flip-angle pulses (for excitation and refocusing) per TR, which is on the order of 80 ms (42). As SAR scales with the square of field strength, SAR increases over 20-fold at 7T relative to 1.5T. The 3D FSE-OSC sequence (18), which is based on variable-amplitude non-selective refocusing pulses, allows operation within SAR limits at 7T, while providing the benefits of a spin-echo sequence. This sequence would be beneficial for TB imaging at 3T as well, where full 180° flip angles could be implemented. Furthermore, at 3T, fatty marrow has a lower T1 value (365 ms) (43) relative to 7T (550 ms) (44) thereby conferring higher SNR efficiency as TR is reduced. In the present implementation of the pulse sequence the bandwidth of the RF excitation pulse was 3.0 KHz. At 7.0T, the fat-water shift is 980 Hz, hence the imaging slab excited for the two constituents (fat and water) is shifted by approximately one third of the slab thickness. However, this is unproblematic since the marrow is entirely fatty at the distal extremities (45). Furthermore, since tissues at the water frequency (e.g., muscle) have reduced intensity due to the non-selective refocusing pulses being tuned to the fat frequency, slice aliasing is of no concern.

Prior work by other investigators studying the potential of high-resolution imaging of trabecular microarchitecture at 7T typically relied on less SAR-intense pulse sequences (13–15,24). In its majority, that work is based on 3D gradient-echo sequences (bSSFP(15) and FLASH (13)) in conjunction with transmit-receive knee coils. The use of a dedicated phased-array receive coil for TB imaging as in our study may have conferred additional gains in SNR. Although both previous studies (15,24) reported an increase in SNR at 7T relative to 3T, given the gradient-echo pulse sequences' sensitivity to chemical shift, susceptibility and off-resonance artifacts in general (all more pronounced at 7T than at lower field), neither study (15,24) has been able to compellingly demonstrate an advantage of 7T for quantitatively imaging TB microarchitecture compared to ongoing work at 3T. To address some of these issues, Krug *et al.*(24) compared image quality and structural parameters between their bSSFP sequence and a newer balanced steady state spin-echo (bSSSE, an analog of FLASE) sequence (scan time: 13 min) with similar voxel size, noting that the spin-echo variant provided a more homogeneous bone marrow signal and finer TB structure due to decreased apparent trabecular thickness. Nevertheless, they found that BVF and Tb.Th values derived from the two types of sequences were highly correlated (24), showing that while significant inter-sequence differences in the structural variables may exist, there is usually high correlation between them.

A limitation of the present study is the short average interval between repeat exams (mean time between repeats ~7 days) in highly compliant, relatively young subjects. Typical longitudinal patient studies designed to evaluate treatment effects are performed at greater intervals (3–12 months) in usually older subjects whose tolerance for relatively long scan times is limited. Therefore, a larger study involving subjects targeted for intervention studies will be needed to corroborate the performance achievable in the test subjects evaluated here. Of interest further would be whether the SNR benefit at 7T can be traded for significantly reduced scan time at the present resolution via parallel imaging with greater reduction factors and without significant loss in image quality and thus detection sensitivity.

It would be of interest to transfer the technology underlying the present study to the distal radius, another peripheral anatomic location that, unlike the distal tibia, is a major fracture site. There are, however, significant practical issues that led us to focus initial development of the technique to the tibia, rather than the radius, namely, (1) the position of the distal radius, which would be off-center in the magnet (a nontrivial issue at 7T), (2) greater potential for subject-induced motion at the wrist (compared to the ankle, which is easier to restrain and immobilize), and 3) the lack of a transmit coil at 7T which would necessitate the development of a dedicated transmit-receive wrist coil. Nevertheless, there is a significant body of data showing correlation of either structural or mechanical parameters between the two distal sites (9). Recent high-resolution MRI studies have further show that the tibia is responsive to drug intervention (9,46).

In conclusion, the new 7T imaging and analysis protocol provides highly reproducible measures of scale, topology and elasticity of trabecular bone microstructure. The improved performance relative to prior MRI-based structure analysis methodology is credited to enhanced SNR, improved subject motion control and correction, and superior retrospective registration techniques. The unique characterization of five healthy subjects based on their TB structural and mechanical parameters underscores the potential utility of these methods to detect treatment-induced microarchitectural and mechanical alterations in clinical settings of diseases such as osteoporosis.

Acknowledgments

Grant Support: NIH RO1 AR53156, RO1 DK75648

References

1. Genant HK, Jiang Y. Advanced imaging assessment of bone quality. Annals of the New York Academy of Sciences. 2006; 1068:410–428. [PubMed: 16831940]
2. Ritchie RO. How does human bone resist fracture? Annals of the New York Academy of Sciences. 2010; 1192(1):72–80. [PubMed: 20392220]
3. Bauer JS, Link TM. Advances in osteoporosis imaging. European journal of radiology. 2009; 71(3): 440–449. [PubMed: 19651482]
4. Griffith JF, Engelke K, Genant HK. Looking beyond bone mineral density: Imaging assessment of bone quality. Annals of the New York Academy of Sciences. 2010; 1192(1):45–56. [PubMed: 20392217]
5. Majumdar S. Magnetic resonance imaging of trabecular bone structure. Top Magn Reson Imaging. 2002; 13(5):323–334. [PubMed: 12464745]
6. Wehrli FW. Structural and functional assessment of trabecular and cortical bone by micro magnetic resonance imaging. J Magn Reson Imaging. 2007; 2:390–409. [PubMed: 17260403]
7. Wehrli FW, Song HK, Saha PK, Wright AC. Quantitative MRI for the assessment of bone structure and function. NMR Biomed. 2006; 19(7):731–764. [PubMed: 17075953]
8. Zhang XH, Liu XS, Vasilic B, et al. In vivo microMRI-based finite element and morphological analyses of tibial trabecular bone in eugonadal and hypogonadal men before and after testosterone treatment. J Bone Miner Res. 2008; 23(9):1426–1434. [PubMed: 18410234]
9. Wehrli FW, Rajapakse CS, Magland JF, Snyder PJ. Mechanical implications of estrogen supplementation in early postmenopausal women. J Bone Miner Res. 2010; 25(6):1406–1414. [PubMed: 20200948]
10. Wehrli FW, Hwang SN, Ma J, Song HK, Ford JC, Haddad JG. Cancellous bone volume and structure in the forearm: noninvasive assessment with MR microimaging and image processing [published erratum appears in Radiology 1998 Jun;207(3):833]. Radiology. 1998; 206:347–357. [PubMed: 9457185]
11. Boutry N, Cortet B, Dubois P, Marchandise X, Cotten A. Trabecular bone structure of the calcaneus: preliminary in vivo MR imaging assessment in men with osteoporosis. Radiology. 2003; 227(3):708–717. [PubMed: 12676974]
12. Banerjee S, Han ET, Krug R, Newitt DC, Majumdar S. Application of refocused steady-state free-precession methods at 1.5 and 3 T to in vivo high-resolution MRI of trabecular bone: simulations and experiments. J Magn Reson Imaging. 2005; 21(6):818–825. [PubMed: 15906346]
13. Regatte RR, Schweitzer ME. Ultra-high-field MRI of the musculoskeletal system at 7.0T. J Magn Reson Imaging. 2007; 25(2):262–269. [PubMed: 17260399]
14. Krug R, Stehling C, Kelley DA, Majumdar S, Link TM. Imaging of the musculoskeletal system in vivo using ultra-high field magnetic resonance at 7 T. Investigative radiology. 2009; 44(9):613–618. [PubMed: 19652609]
15. Krug R, Carballido-Gamio J, Banerjee S, et al. In vivo bone and cartilage MRI using fully-balanced steady-state free-precession at 7 tesla. Magn Reson Med. 2007; 58(6):1294–1298. [PubMed: 17957777]
16. Wald MJ, Magland JF, Rajapakse CS, Wehrli FW. Structural and mechanical parameters of trabecular bone estimated from in vivo high-resolution magnetic resonance images at 3 tesla field strength. J Magn Reson Imaging. 2010; 31(5):1157–1168. [PubMed: 20432352]
17. Banerjee S, Krug R, Carballido-Gamio J, et al. Rapid in vivo musculoskeletal MR with parallel imaging at 7T. Magn Reson Med. 2008; 59(3):655–660. [PubMed: 18224700]
18. Magland JF, Rajapakse CS, Wright AC, Acciavatti R, Wehrli FW. 3D fast spin echo with out-of-slab cancellation: a technique for high-resolution structural imaging of trabecular bone at 7 Tesla. Magn Reson Med. 2010; 63(3):719–727. [PubMed: 20187181]
19. Wang Z, Lin JC, Mao W, Liu W, Smith MB, Collins CM. SAR and temperature: simulations and comparison to regulatory limits for MRI. J Magn Reson Imaging. 2007; 26(2):437–441. [PubMed: 17654736]
20. Hennig J, Friedburg H. Clinical applications and methodological developments of the RARE technique. Magnetic resonance imaging. 1988; 6(4):391–395. [PubMed: 3185132]

21. Park J, Park S, Yeop Kim E, Suh JS. Phase-sensitive, dual-acquisition, single-slab, 3D, turbo-spin-echo pulse sequence for simultaneous T2-weighted and fluid-attenuated whole-brain imaging. Magn Reson Med. 2010; 63(5):1422–1430. [PubMed: 20432315]
22. Stevens KJ, Busse RF, Han E, et al. Ankle: isotropic MR imaging with 3D-FSE-cube--initial experience in healthy volunteers. Radiology. 2008; 249(3):1026–1033. [PubMed: 19011194]
23. Techawiboonwong A, Song H, Saha P, Wehrli F. Implications of pulse sequence in structural imaging of trabecular bone. J Magn Reson Imaging. 2005; 22:647–655. [PubMed: 16215967]
24. Krug R, Carballido-Gamio J, Banerjee S, Burghardt AJ, Link TM, Majumdar S. In vivo ultra-high-field magnetic resonance imaging of trabecular bone microarchitecture at 7 T. J Magn Reson Imaging. 2008; 27(4):854–859. [PubMed: 18383263]
25. Wright, AC.; Wald, M.; Connick, T., et al. 7T transmit four-channel receive array for high-resolution MRI of trabecular bone in distal tibia. Proceedings of the 17th Annual Meeting of ISMRM; Honolulu. 2009. (abstract 256)
26. Wang Z, Wang J, Detre JA. Improved data reconstruction method for GRAPPA. Magn Reson Med. 2005; 54(3):738–742. [PubMed: 16088880]
27. Atkinson D, Hill DL, Stoyle PN, et al. Automatic compensation of motion artifacts in MRI. Magn Reson Med. 1999; 41(1):163–170. [PubMed: 10025625]
28. Lin W, Ladinsky GA, Wehrli F, Song HK. Image metric-based correction (autofocusing) of motion artifacts in high-resolution trabecular bone imaging. J Magn Reson Imaging. 2007; 26:191–197. [PubMed: 17659555]
29. Magland JF, Jones CE, Leonard MB, Wehrli FW. Retrospective 3D registration of trabecular bone MR images for longitudinal studies. J Magn Reson Imaging. 2009; 29(1):118–126. [PubMed: 19097098]
30. Vasilic B, Wehrli FW. A novel local thresholding algorithm for trabecular bone volume fraction mapping in the limited spatial resolution regime of in-vivo MRI. IEEE Trans Med Imaging. 2005; 24:1574–1585. [PubMed: 16353372]
31. Rajapakse CS, Magland JF, Wald MJ, et al. Computational biomechanics of the distal tibia from high-resolution MR and micro-CT images. Bone. 2010; 47(3):556–563. [PubMed: 20685323]
32. Gomberg BG, Saha PK, Song HK, Hwang SN, Wehrli FW. Topological analysis of trabecular bone MR images. IEEE Transactions on Medical Imaging. 2000; 19(3):166–174. [PubMed: 10875701]
33. Saha P, Wehrli F. Measurement of trabecular bone thickness in the limited resolution regime of in vivo MRI by fuzzy distance transform. IEEE Transactions on Medical Imaging. 2004; 23:53–62. [PubMed: 14719687]
34. Magland JF, Wehrli FW. Trabecular bone structure analysis in the limited spatial resolution regime of in vivo MRI. Academic radiology. 2008; 15(12):1482–1493. [PubMed: 19000865]
35. Van Rietbergen B, Odgaard A, Kabel J, Huiskes R. Direct mechanics assessment of elastic symmetries and properties of trabecular bone architecture. Journal of Biomechanics. 1996; 29:1653–1657. [PubMed: 8945668]
36. Gomberg BR, Wehrli FW, Vasilic B, et al. Reproducibility and error sources of micro-MRI-based trabecular bone structural parameters of the distal radius and tibia. Bone. 2004; 35(1):266–276. [PubMed: 15207767]
37. Wehrli FW, Gomberg BR, Saha PK, Song HK, Hwang SN, Snyder PJ. Digital topological analysis of in vivo magnetic resonance microimages of trabecular bone reveals structural implications of osteoporosis. J Bone Miner Res. 2001; 16(8):1520–1531. [PubMed: 11499875]
38. Ladinsky GA, Vasilic B, Popescu AM, et al. Trabecular Structure Quantified With the MRI-Based Virtual Bone Biopsy in Postmenopausal Women Contributes to Vertebral Deformity Burden Independent of Areal Vertebral BMD. J Bone Miner Res. 2008; 23(1):64–74. [PubMed: 17784842]
39. Hildebrand T, Laib A, Muller R, Dequeker J, Ruegsegger P. Direct three-dimensional morphometric analysis of human cancellous bone: microstructural data from spine, femur, iliac crest, and calcaneus. J Bone Miner Res. 1999; 14(7):1167–1174. [PubMed: 10404017]
40. Li CQ, Magland JF, Rajapakse CS, et al. Implications of resolution and noise for in vivo micro-MRI of trabecular bone. Medical physics. 2008; 35(12):5584–5594. [PubMed: 19175116]

41. Newitt DC, van Rietbergen B, Majumdar S. Processing and analysis of in vivo high-resolution MR images of trabecular bone for longitudinal studies: reproducibility of structural measures and micro-finite element analysis derived mechanical properties. Osteoporos Int. 2002; 13(4):278–287. [PubMed: 12030542]

42. Magland JF, Wald MJ, Wehrli FW. Spin-echo micro-MRI of trabecular bone using improved 3D fast large-angle spin-echo (FLASE). Magn Reson Med. 2009; 61(5):1114–1121. [PubMed: 19215044]

43. Gold GE, Han E, Stainsby J, Wright G, Brittain J, Beaulieu C. Musculoskeletal MRI at 3.0 T: relaxation times and image contrast. Ajr. 2004; 183(2):343–351. [PubMed: 15269023]

44. Ren J, Dimitrov I, Sherry AD, Malloy CR. Composition of adipose tissue and marrow fat in humans by 1H NMR at 7 Tesla. Journal of lipid research. 2008; 49(9):2055–2062. [PubMed: 18509197]

45. Cristy M. Active bone marrow distribution as a function of age in humans. Physics in medicine and biology. 1981; 26(3):389–400. [PubMed: 7243876]

46. Benito M, Vasilic B, Wehrli FW, et al. Effect of testosterone replacement on bone architecture in hypogonadal men. J Bone Miner Res. 2005; 20(10):1785–1791. [PubMed: 16160736]

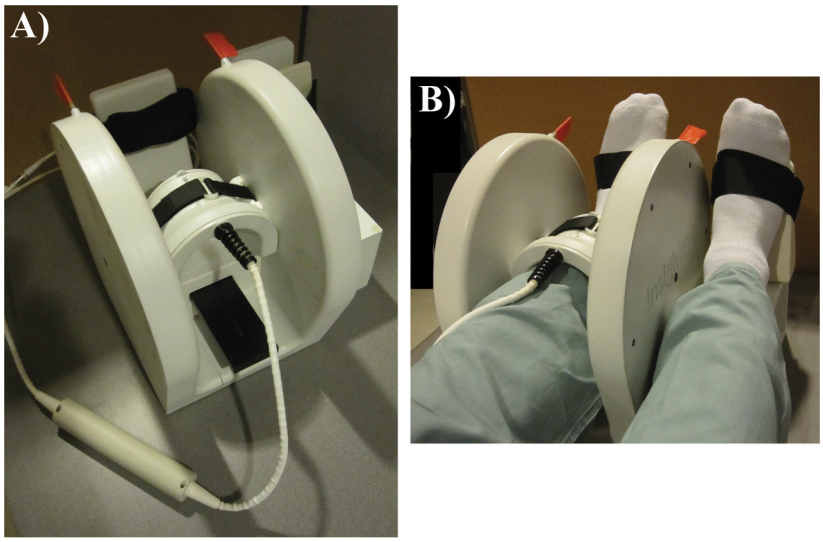

Figure 1.
Imaging setup consisting of (A) a decoupled 4-element phased array receive coil (297.2 MHz) centered within the shielded Helmholtz pair transmit (Tx) coil (Insight MRI, Worcetser, MA). (B) The configuration is shown for imaging a subject's left distal tibia with the right foot positioned on an adjacent platform (outside the Tx coil) of equal height.

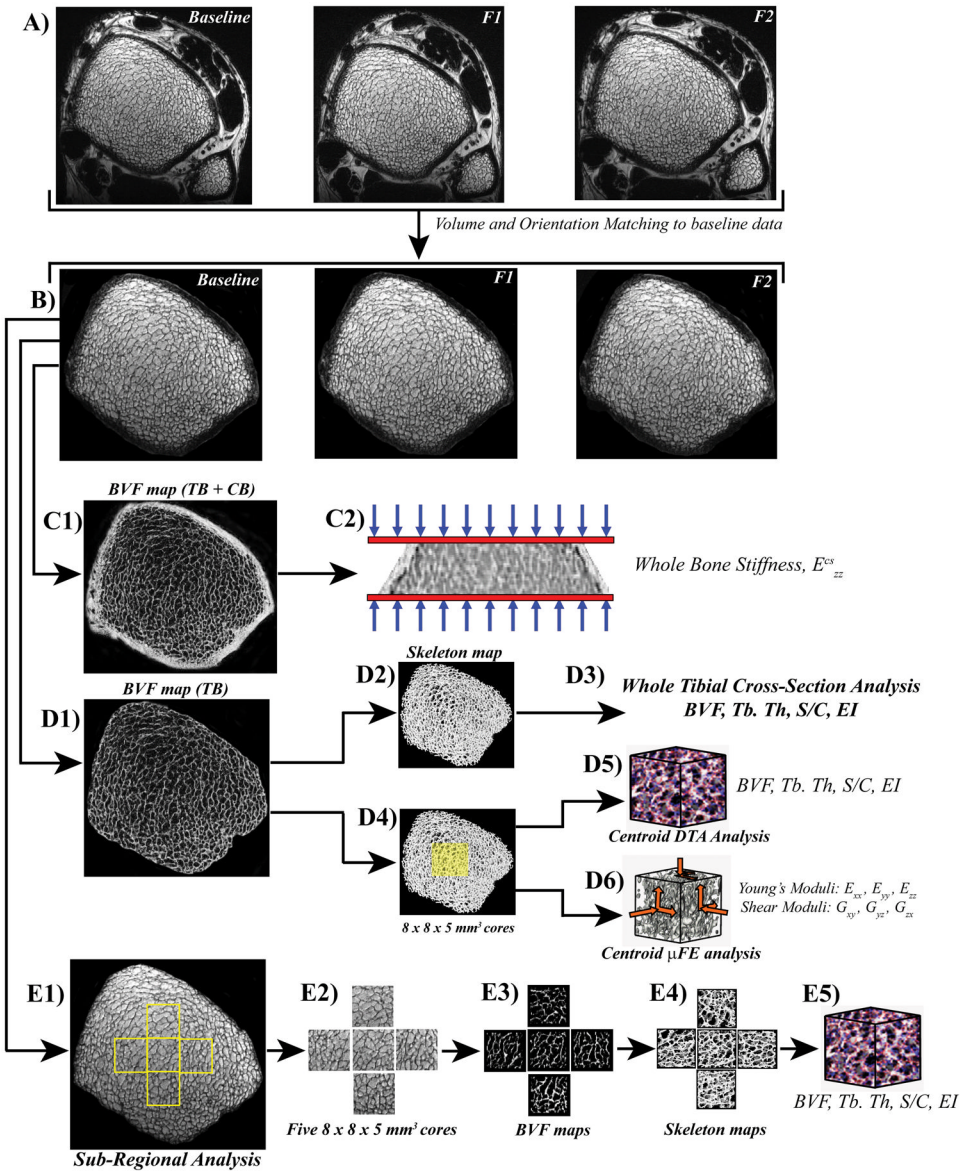

Figure 2.

Image co-registration and virtual bone biopsy processing steps for tibial whole cross-section and sub-regional structural and mechanical parameter analysis. A) *In vivo* μMR images of the distal tibia at 3 time points (baseline, follow-up1 (F1) and Follow-up2 (F2)) from one healthy male subject. B) Images (tibial masks depicting trabecular bone (TB) and cortical bone (CB)) from F1 and F2 are co-registered to the baseline mask using an affine transformation method. C1) Whole section bone volume fraction (BVF) map (TB+CB) serves as an input for micro finite element (μFE) analysis to quantify axial stiffness, E_{zz} (C2). D1) Following whole section segmented BVF mapping (TB only) and skeletonization (D2), parameters of scale and topology such as BVF, trabecular thickness (Tb.Th), surface-to-curve (S/C) ratio and erosion index (EI) are computed (D3). D4) Alternatively, 8 × 8 × 5 mm^3 sub-regional cuboid volumes from the TB center (yellow masks) are analyzed for yielding parameters of scale, topology (D5) and elasticity (D6; Young's and shear moduli from simulated compression and shear FE tests). E1-4) Four additional cubic TB sub-regions (anterior, medial, lateral and posterior (8 × 8 × 5 mm^3)) were extracted and analyzed

to determine associations between whole cross-section and sub-regional structural and topological parameters (E5).

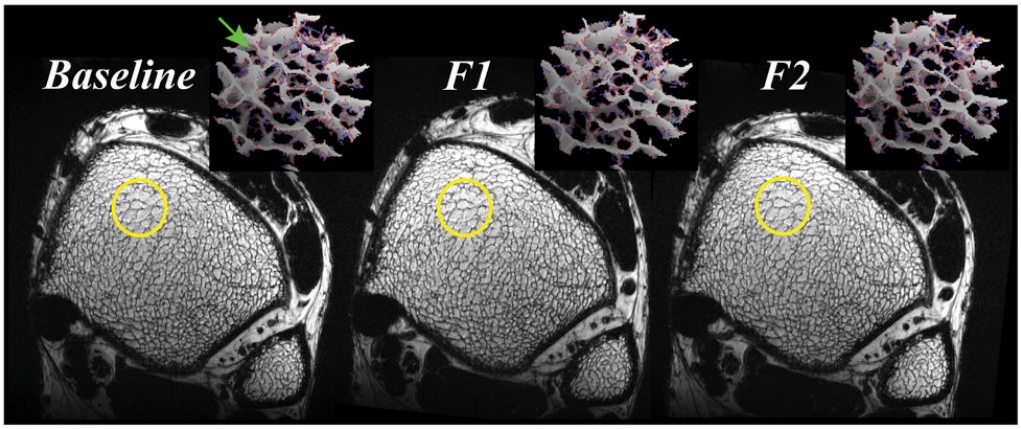

Figure 3.

Representative axial FSE-OSC images of a healthy 36-year-old male subject across the 3 exams. Three dimensional rendered skeletonized virtual cores ($23 \times 23 \times 68$ μm^3 voxels) visually illustrate similarities between plate formations, and minor (green arrow) and major perforations (gray: surface voxels, red: surface edges, blue: curve voxels). Here, 85% of the original baseline volume was retained across the F1 (follow-up 1) and F2 (follow-up 2) time points.

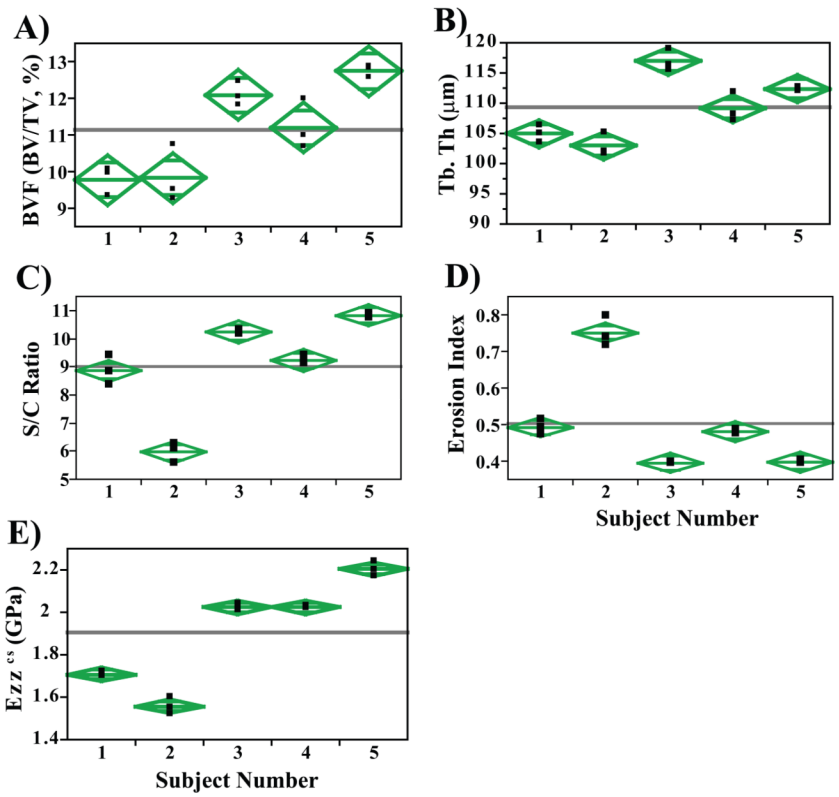

Figure 4.

Scatter plots for (A) Bone volume fraction (BVF), (B) Surface to Curve ratio (S/C), (C) Erosion Index (EI), (D) Axial Stiffness (E_{zz} (GPa), central 5×5×5 mm^3 cuboid), E) Whole bone axial stiffness (E_{zz}^{cs}, GPa) and F) Trabecular thickness (μm) demonstrating the level of longitudinal reproducibility and that the means are significantly different ($p<0.001$) for many pair-wise comparisons (One-way ANOVA). Diamonds highlight the 95% confidence interval about the parameters means.

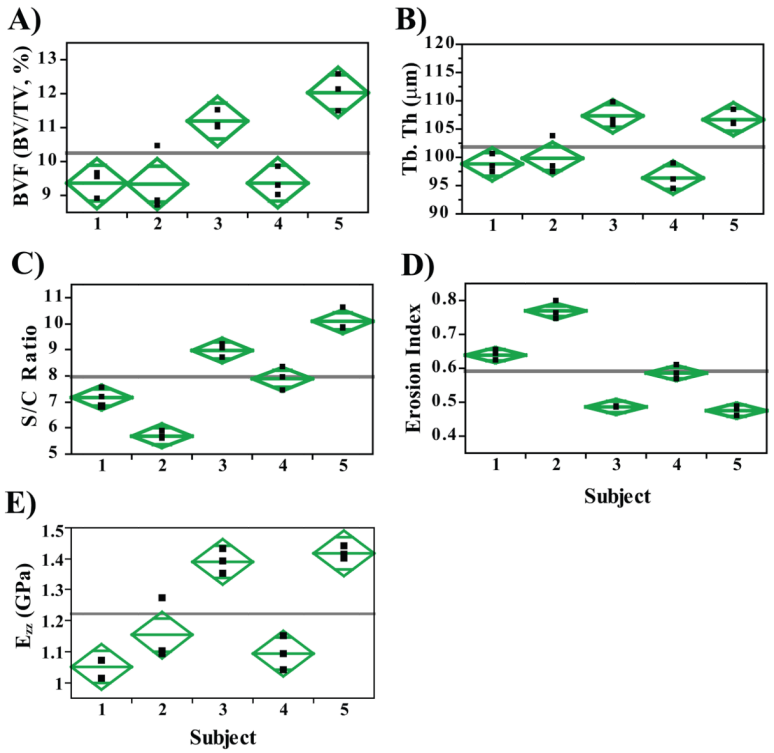

Figure 5.

Scatterplots from sub-regional analysis (central 5 × 5 × 5 mm^3 cuboid) highlighting parameters such as (A) Bone volume fraction (BVF), (B) Surface to Curve ratio (S/C), (C) Erosion Index and (D) Axial Stiffness (E_{zz}, GPa). The level of longitudinal reproducibility is consistent even for a sub-region of the full tibial cross-section (Figure 4). Here too, the topological parameters, S/C and erosion index, serve as better discriminators relative to BVF.

Table 1

Reproducibility measures (means (over all 15 measurements), coefficients of variation (CV) and intra-class correlation coefficients (ICC)) for structural and topological parameters of the full tibial cross section, whole bone (TB+CB) axial stiffness (GPa) and sub-regional ($8 \times 8 \times 5$ mm^3 central cuboid) analysis-based elasticity (GPa) and in 5 normal subjects.

Parameter	Range	Mean	CV(%)	ICC
BVF (%)	[9.2, 12.9]	11.13	4.41	0.95
Tb.Th (μm)	[101.6, 119]	109.30	1.5	0.97
S/C	[5.6, 10.9]	9.02	3.02	0.99
EI	[0.39, 0.80]	0.50	2.44	0.99
E^{cs}_{zz}	[1.52, 2.24]	1.90	1.22	0.99
E_{xx}	[0.27, 0.50]	0.40	4.93	0.98
E_{yy}	[0.29, 0.52]	0.36	4.64	0.98
E_{zz}	[1.01, 1.44]	1.22	4.36	0.96
G_{xy}	[0.14, 0.23]	0.18	4.27	0.97
G_{xz}	[0.20, 0.36]	0.28	4.52	0.98
G_{zy}	[0.21, 0.36]	0.26	4.77	0.98
MA	[2.68, 3.65]	3.26	3.09	0.96

BVF, bone volume fraction; Tb.Th, apparent trabecular thickness; S/C, Surface to curve ratio; EI, erosion index; E^{CS}_{ZZ}, whole cross section (TB+CB) axial stiffness; Young's Moduli (E_{XX}, E_{yy}, and E_{ZZ}); Shear Moduli (G_{XY}, G_{XZ}, G_{ZY}); Mechanical anisotropy, MA = $2E_{ZZ}/(E_{XX}+E_{yy})$

Table 2

Correlations (coefficients of determination, R^2) of Bone volume fraction (BVF), Trabecular thickness (Tb.Th), Surface-Curve (S/C) ratio and Erosion Index (EI) between whole tibial cross section and 5 tibial sub-regions ($8 \times 8 \times 5$ mm^3).

Sub-region	BVF	Tb.Th	S/C	EI
Anterior	0.57†	0.72†	0.77*	0.94**
Center	0.70†	0.58†	0.95**	0.99**
Medial	0.67†	0.70†	0.72†	0.92**
Lateral	0.65†	0.92**	0.64†	0.93**
Posterior	0.72†	0.79*	0.73†	0.95**

The R^2 values are for means from 3 image sets (baseline, follow-up1 and follow-up2) in five test subjects

*, $p<0.05$;

** $p<0.01$;

† not significant.